J. Fluid Mech. (2025), *vol.* 1009, A29, doi:10.1017/jfm.2025.238

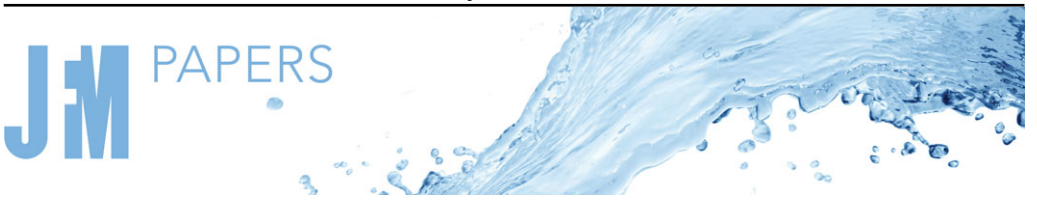

Effects of curvature on turbulent flow in concentric annuli and curved channels

Paolo Orlandi[1], **Giulio Soldati**[1] **and Sergio Pirozzoli**[1]

[1]Dipartimento di Ingegneria Meccanica e Aerospaziale, Sapienza Università di Roma, Via Eudossiana 18, Roma 00184, Italy

Corresponding author: Giulio Soldati, giulio.soldati@uniroma1.it

(Received 10 October 2024; revised 21 January 2025; accepted 24 February 2025)

We investigate turbulent flow between two concentric cylinders, oriented either axially or azimuthally. The axial configuration corresponds to a concentric annulus, where curvature is transverse to the flow, while the azimuthal configuration represents a curved channel with longitudinal curvature. Using direct numerical simulations, we examine the effects of both types of curvature on turbulence, varying the inner radius from $r_i = 0.025\delta$ to $r_i = 95.5\delta$, where δ is the gap width. The bulk Reynolds number, based on bulk velocity and δ, is set at $R_b \approx 5000$, ensuring fully turbulent conditions. Our results show that transverse curvature, although breaking the symmetry of axial flows, induces limited changes in the flow structure, leading to an increase in friction at the inner wall. In contrast, longitudinal curvature has a significant impact on the structure and statistics of azimuthal flows. For mild to moderate longitudinal curvatures ($r_i > 1.5\delta$), the convex wall stabilises the flow, reducing turbulence intensity, wall friction and turbulent kinetic energy (TKE) production. For extreme longitudinal curvatures ($r_i \leqslant 0.25\delta$), spanwise-coherent flow structures develop near the inner wall, leading to a complete redistribution of the TKE budget: production becomes negligible near the inner wall, while pressure–velocity correlations increase substantially. As a result, the mean TKE peaks near the inner wall, thereby weakening the stabilising effect of convex curvature.

Key words: turbulence simulation

1. Introduction

The study of fluid dynamics in cylindrical geometries is fundamental to a wide range of engineering and scientific applications. In systems where fluid is confined between two concentric cylinders, the flow can occur in either the axial or the azimuthal direction. In the

former configuration, known as a concentric annulus, the wall curvature is transverse to the main flow; in the latter, known as a curved channel, the curvature is longitudinal. A clear understanding of how curvature influences axial and azimuthal flows differently is critical for optimising designs across industries, from oil and gas to biomedical engineering.

The former configuration, commonly referred to as Taylor–Poiseuille flow, has significant practical applications, particularly in the context of heat transfer, and has been studied extensively through theoretical, experimental and numerical approaches. In the pioneering work of Rehme (1974), experiments were conducted at small values of the parameter $\alpha = r_i/r_o$, where r_i and r_o are the inner and outer radii of the annulus, respectively. Specifically, he examined the flow cases where $\alpha = 0.02, 0.04, 0.1$. Streamwise velocity profiles were reported for various Reynolds numbers, defined as $Re = D_h u_b/\nu$, where $D_h = 2(r_o - r_i)$ is the hydraulic diameter, u_b is the bulk velocity, and ν is the kinematic viscosity. Rehme (1974) highlighted three critical aspects in his study: (i) the accurate determination of the position of zero shear stress; (ii) the deviations in the location of maximum velocity for radius ratios $\alpha < 0.1$ due to the inherent flow asymmetry in these cases; and (iii) the necessity of obtaining sufficient and reliable experimental data for $\alpha < 0.1$. The range of Reynolds numbers explored in that study is now within the reach of modern direct numerical simulations (DNS). Thus one of the primary objectives of the present study is to revisit and corroborate the experimental findings at low α values, which have not been re-examined since the work of Rehme (1974).

Quadrio & Luchini (2002) performed the first DNS of turbulent flow in a pipe with annular cross-section. Two cases of mild curvature were considered, namely $\alpha = 1/2$ and $\alpha = 1/3$, showing that even a low curvature affects first-order turbulence statistics. Ghaemi *et al.* (2015) investigated turbulent flows in a concentric annular pipe with $\alpha = 0.4$ using particle tracking velocimetry and planar particle image velocimetry. They compared friction velocity values at the inner and outer cylinder walls over a Reynolds number range $Re = 59\,200$ to $90\,800$. Their findings revealed that even at these large values of Re and α, similar to the observations of Rehme (1974) at lower Re and α, the maxima of the streamwise velocity and the location of zero Reynolds shear stress do not coincide. Ghaemi *et al.* (2015) emphasised that this mismatch indicates the presence of a region with negative turbulent kinetic energy (TKE) production. To elucidate the causes of this negative production, they presented budgets of the normal stresses, noting that such behaviour is absent in planar turbulent wall flows. Numerical simulations of turbulent annular flow have also yielded contradictory results on this issue. The DNS conducted by Chung, Rhee & Sung (2002) under conditions similar to those of the experiment by Nouri, Umur & Whitelaw (1993) at $Re = 8900$, demonstrated a non-coincidence between the points where turbulent and viscous shear stresses vanish. However, Boersma & Breugem (2001) reported more recently the coincidence of these two positions in their DNS of fully developed turbulent annular flow with $\alpha = 0.1$ over a Reynolds number range $Re = 8900-13\,940$. They argued that the non-coincidence observed by Chung *et al.* (2002) was likely due to insufficient resolution, and that the discrepancy noted by Rehme (1974) could be attributed to issues with hot-wire calibration. Consistently with the conclusions drawn by Boersma & Breugem (2001), the DNS conducted by Bagheri, Wang & Yang (2020) demonstrated that the zero crossings of the turbulent and viscous stresses coincide. The present study seeks to further clarify this controversy by performing DNS over a broader range of α. Consistent with the findings of Boersma & Breugem (2001), the results show that across all values of α, including the very small $\alpha = 0.025$, there is no region exhibiting negative TKE production.

The occurrence of negative TKE production has never been observed in wall-bounded flows over flat surfaces, but it has been identified by Soldati, Orlandi & Pirozzoli (2025) in

curved channels, a flow configuration similar to concentric annuli, where the main flow is driven in the azimuthal rather than axial direction. Negative production in curved channel flows was first investigated by Eskinazi & Erian (1969), who attributed it to a local 'energy reversal' mechanism, where energy is transferred from turbulent fluctuations back to the mean flow. This reversal in energy production is associated with the formation of large-scale coherent structures near the convex wall of the curved channel (Soldati *et al.* 2025). In the present work, an extensive simulation campaign has been conducted to investigate whether these structures align with the main flow direction or are oriented transversely, depending on the geometry of the configuration. Patel & Head (1969) drew an analogy between the effects of convex curvature and adverse pressure gradients on boundary layers, noting that in the latter configuration, spanwise rollers may appear downstream of the reattachment point. This phenomenon is akin to the enhanced inflectional instability compared to wake instability, demonstrating that two-dimensional tripping devices are more effective in promoting the transition from laminar to turbulent flow in boundary layers, as documented by the experiments of Erm & Joubert (1991).

Some of the most relevant studies on flows between a convex and a concave wall are reported in Soldati *et al.* (2025). Their work documents peculiar features of the flow near the convex wall, in terms of both flow structure and the behaviour of the friction coefficient C_f as a function of the bulk Reynolds number $R_b = u_b\delta/\nu$, where $\delta = r_o - r_i = D_h/2$. In that study, DNS were conducted over a wide range of R_b, covering mild to strong channel curvatures, which had not been explored previously. The mildly curved channel with curvature radius $r_c = 39.5\delta$, where $r_c = (r_o + r_i)/2$, was first investigated via DNS by Moser & Moin (1987) at $R_b = 5200$. Subsequent DNS studies of turbulent flow in mildly curved channels followed, including the work of Nagata & Kasagi (2004) at $R_b = 4600$, and of Brethouwer (2022) at $R_b = 40\,000$. In these studies, moderate channel curvatures were also considered: Nagata & Kasagi (2004) explored curvature ratio $r_c = 2.5\delta$, while Brethouwer (2022) reached $r_c = 3\delta$. Figure 1 in the study by Soldati *et al.* (2025) presents the values of R_b and r_c/δ considered in previous experiments and DNS, showing that very strong curvatures, specifically $r_c < \delta$, comparable to those studied in annular pipe flows, had never been explored in curved channel flows. From the plots of C_f versus R_b reported in Soldati *et al.* (2025), it can be inferred that a Reynolds number $R_b \approx 5000$ is sufficiently large to capture interesting turbulent behaviours associated with variations in curvature radius, while still being small enough to permit the use of a limited number of grid points, thus minimising computational costs.

The paper is organised as follows. First, the flow physics at very small values of inner radius r_i, which has not been investigated deeply, is highlighted through profiles of total and normal stresses. Focusing on azimuthal flows, the TKE budgets are evaluated, showing that near the convex wall, production decreases as r_i decreases, and total dissipation balances the strong positive contribution of the pressure work term. This suggests that the fluctuating pressure plays an increasingly important role as the inner radius decreases, as confirmed by the instantaneous visualisations, which are shown to clarify how the flow is organised as the curvature changes. Finally, the correlations between fluctuating pressure and radial velocity are analysed, elucidating the role of radial velocity and the transverse structures formed in azimuthal flow for small values of the inner radius. This paper is closely linked to the work by Soldati *et al.* (2025), specifically targeting Reynolds number effects in curved channel flow, which revealed intriguing behaviour at intermediate values of R_b, for given $r_c = \delta$. The present study delves into additional flow complexity arising at even lower values of r_i. We acknowledge that replicating this flow configuration in laboratory experiments involving azimuthal pressure-driven flows is nearly impossible. Therefore, the observations reported herein may be regarded

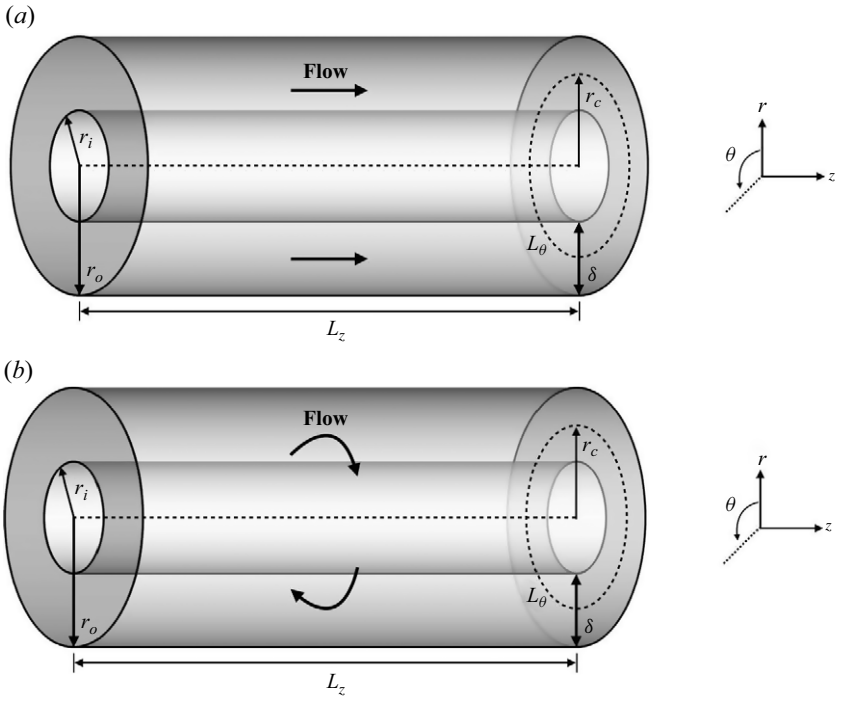

Figure 1. Computational set-up for (*a*) axial flows and (*b*) azimuthal flows.

as of mainly academic or speculative interest. However, the study can still serve as a useful database for scholars employing different numerical methods. In fact, some researchers have encountered difficulties with numerical methods similar to ours when considering curved channels with small internal radii (personal communication). For practical implementation and verification of our findings, we believe that it is worthwhile to perform numerical experiments on Taylor–Couette flows with internal radii as small as 0.02δ to assess whether turbulence exhibits behaviour similar to that observed for pressure-driven azimuthal flows. Taylor–Couette flow might be a more suitable candidate for laboratory studies, although challenges remain in achieving accurate measurements of friction factors, velocity profiles and flow visualisations.

2. Methodology

The computational domain is bounded by sectors of concentric cylinders, as shown in figure 1(*a*) for the concentric annulus (axial flows) and in figure 1(*b*) for the curved channel (azimuthal flows). The velocity components along the azimuthal (θ), radial (r) and axial (z) directions are denoted by v_θ, v_r and v_z, respectively. The axial flow in the annulus is driven by a mean pressure gradient ($\partial P/\partial z$), imposed as a volumetric forcing to maintain a constant mass flow rate over time. Similarly, for the azimuthal flow a mean pressure gradient ($\partial P/\partial\theta$) is required to achieve a constant mass flow rate in the azimuthal direction. In both types of flow, no-slip boundary conditions are applied on the internal and external cylindrical walls, and periodicity is assumed in the θ- and z-directions. The statistical steady state is reached when the mean pressure gradient, which balances the wall friction, oscillates around a mean value.

The incompressible Navier–Stokes equations in cylindrical coordinates are solved using a second-order finite-difference scheme developed by Verzicco & Orlandi (1996). This scheme employs $q_r = r v_r$ as a computational variable, which simplifies the treatment of the axis in the computational domain. Although this assumption is not necessary for the present set-up, it is retained as the code employed here is the same as that used for DNS of pipe flow by Orlandi & Fatica (1997). The governing equations are advanced in time using a hybrid third-order low-storage Runge–Kutta algorithm, where the diffusive terms are treated implicitly, and the convective terms are treated explicitly.

Throughout the following discussion, it is implied that all lengths are scaled by $\delta = r_o - r_i$, and velocities by u_b. For small values of inner radius, specifically $r_i < 2.5$, the continuity and momentum equations are solved for the variable $q_\theta = r v_\theta$. For $r_i > 2.5$, instead, the v_θ equation is discretised. When the azimuthal flow is considered, the mean pressure gradient is expressed as $\partial P/\partial\theta$ in the q_θ-formulation, whereas in the v_θ-formulation it is expressed as $(\partial P/\partial\theta)/r$, where $\partial P/\partial\theta$ is constant. Consequently, the volumetric forcing varies along the radial direction when the variable v_θ is considered. A second version of the code, written in the v_θ-formulation, has been used for the flow cases with $r_i < 2.5$ to validate the results obtained with the q_θ-formulation. This version has been adapted to run on clusters of graphic accelerators (GPUs), utilising a combination of CUDA Fortran and OpenACC directives, and relying on the CUFFT libraries for efficient execution of fast Fourier transforms. The balance equations written in the q_θ-formulation read as follows.

Continuity equation:

$$\frac{\partial q_r}{\partial r} + \frac{1}{r}\frac{\partial q_\theta}{\partial \theta} + r\frac{\partial q_z}{\partial z} = 0. \tag{2.1}$$

Transport equation for q_θ:

$$\begin{aligned}&\frac{\partial q_\theta}{\partial t} + \frac{\partial q_\theta/r q_r}{\partial r} + \frac{1}{r^2}\frac{\partial q_\theta^2}{\partial \theta} + \frac{\partial q_\theta q_z}{\partial z} + \frac{q_\theta}{r}\frac{q_r}{r} \\ &= -\frac{\partial p}{\partial \theta} - \overline{\frac{\partial P}{\partial \theta}}\delta_{i\theta} + \frac{1}{Re}\left[\nabla^2 q_\theta - \frac{2}{r}\frac{\partial q_\theta}{\partial r} + \frac{2}{r^2}\frac{\partial q_r}{\partial \theta}\right].\end{aligned} \tag{2.2}$$

Transport equation for q_r:

$$\begin{aligned}&\frac{\partial q_r}{\partial t} + \frac{\partial}{\partial r}\frac{q_r^2}{r} + \frac{\partial}{\partial \theta}\frac{q_\theta q_r}{r^2} + \frac{\partial q_r q_z}{\partial z} - \frac{q_\theta^2}{r^2} \\ &= -r\frac{\partial p}{\partial r} + \frac{1}{Re}\left[\nabla^2 q_r - \frac{2}{r}\frac{\partial q_r}{\partial r} - \frac{2}{r^2}\frac{\partial q_\theta}{\partial \theta}\right].\end{aligned} \tag{2.3}$$

Transport equation for q_z:

$$\begin{aligned}&\frac{\partial q_z}{\partial t} + \frac{1}{r}\frac{\partial q_r q_z}{\partial r} + \frac{1}{r^2}\frac{\partial q_\theta q_z}{\partial \theta} + \frac{\partial q_z^2}{\partial z} \\ &= -\frac{\partial p}{\partial z} - \overline{\frac{\partial P}{\partial z}}\delta_{iz} + \frac{1}{Re}\left[\nabla^2 q_z\right].\end{aligned} \tag{2.4}$$

In these equations, the Laplacian is expressed as

$$\nabla^2 q = \frac{\partial^2 q}{\partial z^2} + \frac{1}{r}\frac{\partial}{\partial r}\left(r\frac{\partial q}{\partial r}\right) + \frac{1}{r^2}\frac{\partial^2 q}{\partial \theta^2}. \tag{2.5}$$

Axial flows

r_i	α	N_θ	N_r	N_z	L_θ	L_z	$R_b \times 10^{-4}$	$C_{f,i} \times 10^2$	$C_{f,o} \times 10^2$	ΔP_N
0.0250	0.0244	384	256	384	6.28	8.0	0.538	2.05	0.690	0.0
0.0500	0.0476	384	256	384	6.28	8.0	0.526	1.52	0.708	0.0
0.0750	0.0698	384	256	384	6.28	8.0	0.522	1.32	0.720	0.0
0.125	0.111	384	256	384	6.28	8.0	0.515	1.12	0.733	0.0
0.250	0.200	256	256	384	6.28	8.0	0.509	0.988	0.755	0.0
0.500	0.333	512	256	512	6.28	8.0	0.504	0.916	0.770	0.0
0.750	0.429	512	256	512	6.28	8.0	0.502	0.892	0.788	0.0
1.00	0.500	512	256	512	3.14	8.0	0.501	0.875	0.788	0.0
2.50	0.714	512	256	512	3.14	8.0	0.499	0.846	0.810	0.0
5.50	0.846	512	256	512	2.09	8.0	0.499	0.837	0.822	0.0
14.5	0.935	512	256	512	0.785	8.0	0.499	0.835	0.828	0.0
24.5	0.961	512	256	512	0.449	8.0	0.499	0.831	0.828	0.0
40.0	0.976	256	128	512	0.157	8.0	0.499	0.833	0.829	0.0
59.5	0.983	512	128	512	0.209	8.0	0.499	0.830	0.829	0.0
79.5	0.988	512	128	512	0.157	8.0	0.499	0.832	0.829	0.0
95.5	0.990	512	128	512	0.126	8.0	0.499	0.830	0.829	0.0

Azimuthal flows

r_i	α	N_θ	N_r	N_z	L_θ	L_z	$R_b \times 10^{-4}$	$C_{f,i} \times 10^2$	$C_{f,o} \times 10^2$	$10\,\Delta P_N$
0.0250	0.0244	384	128	512	6.28	8.0	0.743	1.14	0.549	0.432
0.0500	0.0476	384	128	512	6.28	8.0	0.709	1.06	0.601	0.584
0.0750	0.0698	384	128	512	6.28	8.0	0.678	1.01	0.658	0.659
0.125	0.111	384	128	384	6.28	8.0	0.569	0.932	0.847	0.808
0.250	0.200	512	256	512	6.28	8.0	0.550	0.802	0.998	1.09
0.500	0.333	512	256	512	6.28	8.0	0.516	0.713	1.18	1.06
0.750	0.429	512	256	512	6.28	8.0	0.507	0.654	1.24	1.02
1.00	0.500	512	256	512	3.14	8.0	0.502	0.616	1.25	0.815
1.50	0.600	512	256	512	3.14	8.0	0.497	0.572	1.26	0.559
2.50	0.714	512	256	512	3.14	8.0	0.498	0.534	1.22	0.257
5.50	0.846	384	128	384	2.09	8.0	0.496	0.489	1.15	0.264
9.50	0.905	384	128	384	1.05	8.0	0.497	0.485	1.07	0.598
14.5	0.935	512	256	512	0.785	8.0	0.497	0.476	1.04	1.00
24.5	0.961	384	128	384	0.449	4.0	0.498	0.542	1.00	1.40
40.0	0.976	256	128	256	0.157	4.0	0.498	0.637	0.932	0.639
59.5	0.983	512	128	256	0.209	4.0	0.498	0.718	0.912	0.251
79.5	0.988	512	128	256	0.157	4.0	0.498	0.760	0.887	0.0612
95.5	0.990	512	128	256	0.126	4.0	0.499	0.767	0.877	0.0482

Table 1. Flow parameters: inner radius (r_i), inner to outer radii ratio (α), number of grid points in the azimuthal (N_θ), radial (N_r) and axial (N_z) directions, domain sizes in the azimuthal (L_θ, expressed in radians) and axial (L_z) directions, bulk Reynolds number (R_b), friction coefficient at the inner ($C_{f,i}$) and outer ($C_{f,o}$) walls, radial extent of the layer with negative TKE production (ΔP_N).

Two sets of simulations have been performed, one with the flow along the axial direction ($i = z$ and $\delta_{zz} = 1$), and the other along the azimuthal direction ($i = \theta$ and $\delta_{\theta\theta} = 1$). The flow parameters of all simulations are listed in table 1. As shown, the inner radius ranges from the very small value $r_i = 0.025$ (strong curvature) up to the rather large value $r_i = 95.5$ (mild curvature), which are respectively smaller and greater than the values considered in previous simulations. Variations in curvature lead to different behaviours near the inner (convex) and outer (concave) wall. Domain sizes and numbers of grid points, as well as the resulting bulk Reynolds number, are listed in table 1 for each simulation. A distinction between the inner and outer wall is necessary because the friction velocity

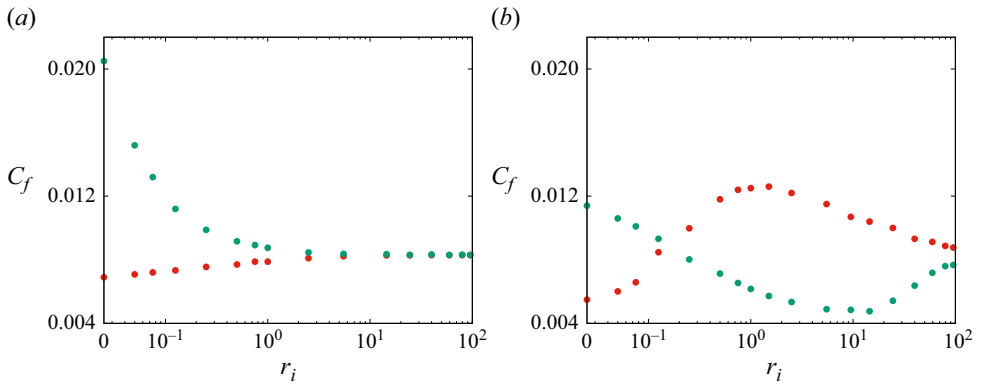

Figure 2. Friction coefficient at the inner wall ($C_{f,i}$, green) and at the outer wall ($C_{f,o}$, red) versus the inner radius for (*a*) axial flows and (*b*) azimuthal flows.

varies depending on the wall at which it is computed, due to the asymmetry of the mean velocity profile. The non-dimensional friction velocities at the inner and outer wall are defined as

$$u_{\tau,i} = \sqrt{\frac{1}{R_b}|\frac{\partial U}{\partial r}|_{r_i}} = \tau_{w,i}^{1/2}, \quad u_{\tau,o} = \sqrt{\frac{1}{R_b}|\frac{\partial U}{\partial r}|_{r_o}} = \tau_{w,o}^{1/2}. \tag{2.6}$$

In these equations, the mean velocity is $U = \overline{v_z}$ for flows along the axial direction, and $U = \overline{v_\theta}$ for flows along the azimuthal direction, where the overline indicate that the variable is averaged in the homogeneous spatial directions and in time.

3. Results

3.1. *Friction coefficient*

The friction coefficient is a key parameter for characterising the influence of the curvature radius on flows in concentric annuli and curved channels. Based on the friction velocities (2.6), we define friction coefficients at the inner and outer wall as

$$C_{f,i} = 2\left(\frac{u_{\tau,i}}{u_b}\right)^2, \quad C_{f,o} = 2\left(\frac{u_{\tau,o}}{u_b}\right)^2, \tag{3.1}$$

which are listed in table 1 and shown in figure 2, as a function of the inner radius. For axial flows (figure 2*a*), there is a significant decrease in friction at the inner wall (green dots) as r_i increases, accompanied with moderate increase at the outer wall (red dots). This can be explained by looking at the mean axial velocity profiles (not shown here), whose maxima shift towards the inner wall as r_i decreases. The friction difference between two walls decreases as the inner radius increases, vanishing for $r_i > 2.5$. Quadrio & Luchini (2002) evaluated the overall resistance of the two walls by weighting their friction coefficients with the corresponding wetted areas, and noticed that the overall friction is essentially unchanged from its planar value, for $r_i \geqslant 1$. The data in table 1 do confirm this behaviour, at least for $r_i \geqslant 1$. However, the overall drag increases for smaller r_i. This suggests that when wall curvature is transverse to the mean flow, the effects of concave and convex walls are significant only when the inner radius of the annulus is small compared to the distance between the two walls.

For azimuthal flows (figure 2*b*), the friction trend at the two walls is more complex. In particular, $C_{f,i}$ has a minimum at $r_i \approx 14.5$, $C_{f,o}$ has a maximum at $r_i \approx 1.5$, and there is a crossover of friction at the two walls at $r_i \approx 0.25$. At very large values of r_i, $C_{f,i}$ is slightly less than $C_{f,o}$, with a difference of approximately 10 %. This behaviour allows us to identify four flow regimes, namely: (i) mild curvature for $r_i > 14.5$; (ii) moderate curvature for $1.5 < r_i \leqslant 14.5$; (iii) strong curvature for $0.25 < r_i \leqslant 1.5$; (iv) extreme curvature for $r_i \leqslant 0.25$.

In these simulations, the bulk Reynolds number is set to $R_b = 5000$, which is sufficiently high to result in fully turbulent flow conditions. Soldati *et al.* (2025) found that for mildly curved channels ($r_i = 40$), the friction at the inner wall is permanently lower than at the outer wall as the Reynolds number increases. In contrast, for strongly curved channels ($r_i = 0.5$), the friction at the inner wall exceeds that at the outer wall for $R_b < 1000$, and becomes lower for higher R_b. Figure 2(*b*) displays a similar behaviour, with crossing point at $r_i \approx 0.25$. The maximum difference between the friction at the two walls is obtained for $r_i = 2.5$, at which $C_{f,o}$ is more than twice $C_{f,i}$.

This complex behaviour arises in azimuthal flows because of two competing effects. First, as the curvature radius is reduced, destabilisation at the outer wall and stabilisation at the inner wall yield, respectively, increase and decrease of the friction coefficient. By further reducing the inner radius, the wetted area of the inner wall becomes very small, such that the maximum velocity (not shown here) approaches it, with consequent tendency for the friction coefficient to increase at the inner wall. The inversion of friction at the two walls occurring in azimuthal flows will be further characterised through the analysis of the TKE transport equation, which reveals the dominance of the pressure–velocity correlation term and a reduction in production.

3.2. *Total stress and turbulent energy production*

The expressions for the total stress in the concentric annulus and curved channel configurations are given by

$$\tau_{T,z} = \frac{1}{Re}\frac{\partial \overline{v_z}}{\partial r} - \overline{v_z' v_r'}, \qquad \tau_{T,\theta} = \frac{1}{Re}\frac{r\,\partial(\overline{v_\theta}/r)}{\partial r} - \overline{v_\theta' v_r'}, \tag{3.2}$$

respectively, where the fluctuating velocities are defined as $v_i' = v_i - \overline{v_i}$. Given the large number of configurations investigated, only a selection of flow cases is displayed in figure 3, specifically those with $r_i = 0.025$, 0.125, 1, 5.5, 14.5 and 79.5, for both axial (figure 3*a*) and azimuthal (figure 3*b*) flows. The achievement of smooth profiles indicates that a good statistical steady state has been reached. For azimuthal flows, Brethouwer (2022) derived the following analytical expression for the total stress profile:

$$\tau_{T,\theta}(r) = \frac{r_i^2 \tau_{w,i}(r_o^2 - r^2) + r_o^2 \tau_{w,o}(r_i^2 - r^2)}{2r^2 r_c \delta}. \tag{3.3}$$

The azimuthal flow cases with extreme value of curvature, namely $r_i = 0.025$ (red) and $r_i = 0.125$ (green), exhibit a total stress profile that deviates more significantly from a linear trend. In figure 3(*b*), we report the analytical profile (3.3) for these two cases (open circles), which shows excellent agreement with the computed profiles (dots), further indicating well-converged statistics.

In wall-bounded flows, TKE production typically scales well with wall friction, especially as the Reynolds number increases. For smooth, flat walls, this production reaches a maximum value of approximately 0.25 in wall units, located at a fixed distance from the wall (Pope 2000). However, the stabilising effect of the convex wall leads to a

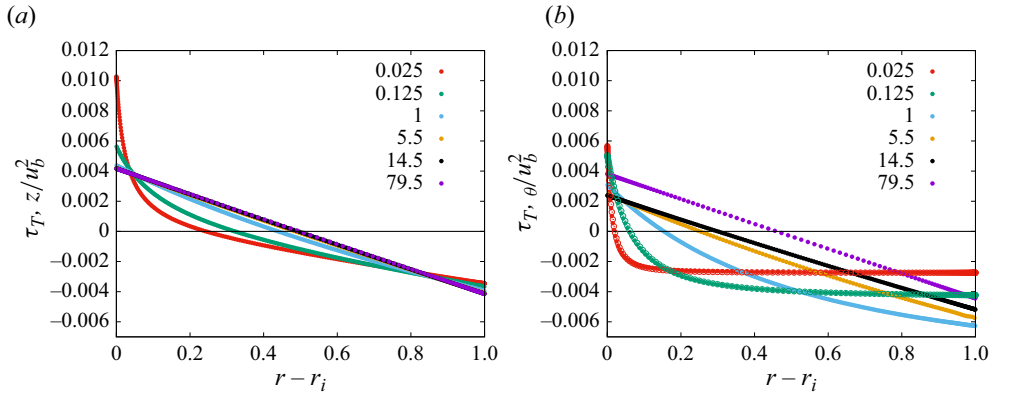

Figure 3. Total stress profiles scaled by bulk velocity versus distance from inner wall for (*a*) axial flows and (*b*) azimuthal flows. The values of r_i are reported in the legend. The open circles denote the analytical profiles of $\tau_{T,\theta}(r)/u_b^2$ from (3.2) for the azimuthal flow cases with $r_i = 0.025$ and $r_i = 0.125$.

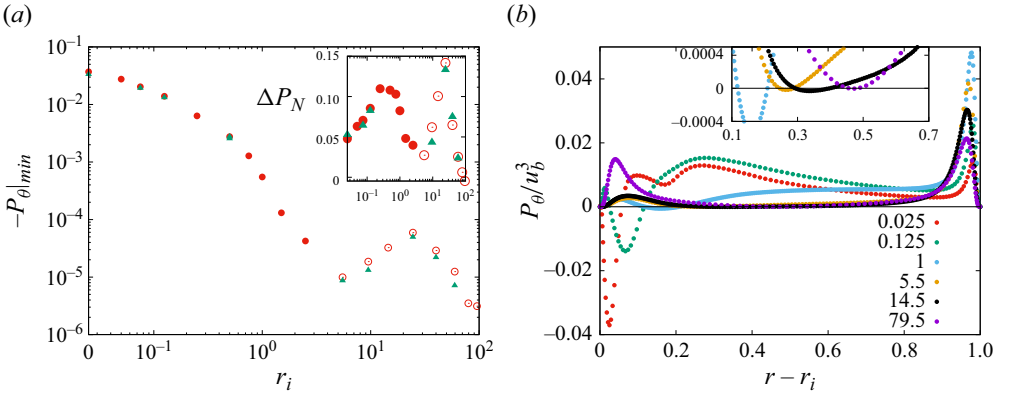

Figure 4. (*a*) Minimum of negative production ($-P_\theta|_{min}$) versus the inner radius; in the inset, the thickness ΔP_N of the layer with $P_\theta < 0$ is plotted versus r_i. Red dots denote results obtained with the rv_θ-formulation, red circles with the v_θ-formulation, and green triangles with the GPU-version of the v_θ-formulation. (*b*) Profiles of TKE production scaled by bulk velocity versus distance from the inner wall; the inset shows a close-up view of the production profiles for flow cases with $r_i > 1$. The values of r_i are reported in the legend. Both plots refer to azimuthal flows.

reduction in TKE production, which may even become negative, implying a transfer of energy from turbulent fluctuations to the mean flow. As mentioned in the Introduction, there has been a debate regarding the existence of a layer with negative TKE production in concentric annulus flows. The last column of table 1 reports the mean extent in the radial direction of the flow region where production is negative, which we define as ΔP_N. For axial flows, ΔP_N is zero for all values of the inner radius, confirming the conclusions drawn by Boersma & Breugem (2001). In contrast, a completely different behaviour is observed for azimuthal flows, for which a negative production layer exists at each value of r_i.

This point is further investigated in figure 4(*a*), which focuses on azimuthal flows and illustrates the minimum of $P_\theta = -\overline{v_\theta' v_r'}\, r\, \partial(U_\theta/r)/\partial r$ in absolute value as a function of the inner radius. The figure highlights the large values of negative production for small

r_i, and its sharp reduction as r_i increases. A local maximum is observed for $r_i = 24.5$; however, the semi-logarithmic scale amplifies values that are actually extremely lower than those obtained for small r_i. The inset of figure 4(*a*) shows the extent of the layer with negative production ΔP_N, also listed in table 1. Notably, ΔP_N increases for large values of the inner radius, specifically between $r_i = 9.5$ and $r_i = 40$. However, these relatively high values of ΔP_N are not as significant as those observed for small r_i. This can be inferred from figure 4(*b*), where the profiles of P_θ are shown for the same flow cases as in figure 3(*b*): the broad layer with negative production observed for large r_i corresponds to negative values of P_θ that are nearly zero.

The profiles of P_θ in figure 4(*b*) further characterise the occurrence of negative TKE production in azimuthal flows. Near the outer wall, P_θ is always positive, though the amplitude of its peak varies in a complex manner. For $r_i = 1$, at which the peak amplitude is maximum, the high turbulence activity near the outer wall influences the channel core, but does not affect significantly the layer near the inner wall, where the stabilising effect of convex curvature tends to suppress P_θ. For flow cases with $r_i > 1$, the peak production near the outer wall decreases in amplitude with r_i, whereas it increases near the inner wall, without reaching the value near the outer wall. For values $r_i < 1$, production increases in the channel core, and decreases to large negative values near the inner wall. Since the production is inherently related to the flow structures, the complex profiles of P_θ indicate a modification of the flow structures for the azimuthal flow cases with $r_i < 1$, which will be stressed in the following through a detailed analysis of the budget terms in the TKE transport equation.

3.3. *Velocity and pressure correlations*

As can be inferred from the results presented so far, identifying a suitable scaling for both the mean velocity and the normal stresses with respect to the friction velocities at the two walls is quite challenging. Thus we consider the normalised anisotropy tensor b_{ij}, which is typically defined as $b_{ij} = \overline{v_i' v_j'}/\overline{K} - 1/3\delta_{ij}$, where $\overline{K} = 2\overline{K'}$ is twice the mean TKE. Here, we adopt an alternative definition, normalising each component of the anisotropy tensor by its maximum value, namely $b_{ij} = \overline{v_i' v_j'}/\overline{v_i' v_j'}|_{max}$, in such a way that quantities range between 0 and 1. This definition allows for the fluctuating pressure correlations, which we define as $b_{pp} = \overline{p'p'}/\overline{p'p'}|_{max}$ consistently with b_{ij}, to be visualised on the same plot.

Examining the profiles of the diagonal components b_{ii} in the present configurations can reveal whether wall curvature enhances or diminishes flow anisotropy with respect to flat walls, for which b_{ii} exhibit strong inhomogeneity near the wall, and a fair isotropy farther from the wall. To facilitate comparison between flow over curved and flat walls, we provide in figure 5 the profiles of b_{ii} obtained from the data by Lee & Moser (2015) for plane channel flow at various friction Reynolds numbers (R_τ), specifically $R_\tau = 180, 550, 1000, 2000, 5200$. These data reveal that in the buffer region, the streamwise (red dots) and spanwise (orange dots) components exhibit a maximum, whose location is independent of the friction Reynolds number for $R_\tau > 500$. In fact, the only profiles that do not collapse on the others in the viscous wall region are those at $R_\tau = 180$ (solid lines). Regarding the pressure fluctuations, the values of b_{pp} (black) show a Reynolds number dependence, but the peak location remains invariant.

For curved wall configurations, we report in figure 6 the profiles of b_{ii} and b_{pp} for axial flows (left-hand panels) and azimuthal flows (right-hand panels) with $r_i = 0.125$ (figures 6*a*,*b*), $r_i = 1$ (figures 6*c*,*d*), and $r_i = 79.5$ (figures 6*e*,*f*). To facilitate a quick comparison between the two flow configurations, the components along the flow direction

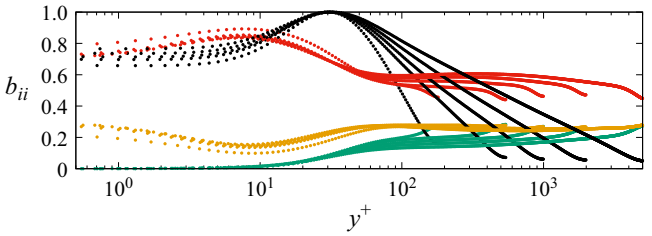

Figure 5. Diagonal components of the anisotropy tensor (streamwise in red, wall-normal in green, and spanwise in orange) and fluctuating pressure correlations (in black) scaled by their maximum values. Profiles obtained by Lee & Moser (2015) for plane channel flow at friction Reynolds numbers $R_\tau = 180$ (lines), and $R_\tau = 550$, 1000, 2000, 5200 (dots).

are plotted in red, namely $b_{\theta\theta}$ for flow in the θ-direction, and b_{zz} for flow along the z-direction. The three panels on the left-hand side for axial flows show similar trends with minor differences. For $r_i = 79.5$ (figure 6*e*), a fairly good symmetry is observed for all quantities. Comparing figure 6(*e*) and figure 5, some differences in amplitude are observed. These differences are due to the Reynolds number, which is $R_\tau \approx 160$ in the present simulations for $r_i = 79.5$. For $r_i = 1$ (figure 6*c*), the symmetry of the flow breaks down, as is visible from the minimum of b_{zz}, b_{pp} and the maximum of b_{rr}, $b_{\theta\theta}$ in the central region shifting slightly towards the inner wall. This trend is even more pronounced for $r_i = 0.125$ (figure 6*a*). For axial flows, the maximum of b_{pp} remains fixed near the outer wall, whereas its peak near the inner wall diminishes in amplitude with r_i, decreasing to half the absolute maximum for $r_i = 0.125$ (figure 6*a*). The minimum of b_{pp} is located at the same position where b_{rr} is maximum.

For the azimuthal flow case with $r_i = 79.5$, the profiles of b_{ii} in figure 6(*f*) do not differ significantly from those in figure 6(*e*) for the axial flow in the same geometry. However, a slight asymmetry is present, which is particularly evident in the profile of b_{pp}. This suggests that even a small curvature in the longitudinal direction influences the normal stresses and especially the fluctuating pressure. As for axial flows, the maximum of b_{pp} is located near the outer wall for large values of the inner radius. All the profiles change drastically for azimuthal flows with small values of the inner radius. At $r_i = 1$ (figure 6*d*), a significant increase in b_{rr} is observed with respect to the corresponding axial flow case in figure 6(*c*). This increase in radial velocity fluctuations, more pronounced towards the outer wall, is explained by the presence of large ejections that influence the flow structures near the outer wall, as will be shown in the following through flow visualisations. These large-scale ejections are also responsible for the large values near the outer wall of total stress and TKE production, both reaching their peak for $r_i = 1$ (cyan dots in figures 3*b* and 4*b*). In a small layer around $r - r_i \approx 0.9$, the flow tends to be isotropic due to a strong reduction in $b_{\theta\theta}$. This small layer of isotropic flow near the outer wall is also characterised by the absence of a distinct peak in b_{pp}. The reduction of $b_{\theta\theta}$ is even stronger near the inner wall, explaining the sharp reduction of P_θ in that region (cyan dots in figure 4*b*). Together with the formation of a prominent peak in b_{pp} near the inner wall, this suggests a complete rearrangement of the budgets in the TKE transport equation. For the azimuthal flow case with $r_i = 0.125$, what emerges from figure 6(*b*) is a large peak of b_{rr} near the inner wall, in correspondence with the maximum of b_{pp}. The presence of this peak in radial velocity fluctuations suggests that the rearrangement of the TKE budgets is even more marked for this flow case with extreme curvature, as discussed in the next subsection.

The results obtained so far indicate that transverse curvature does not alter substantially the structure of axial flows with respect to canonical wall-bounded flows, whereas

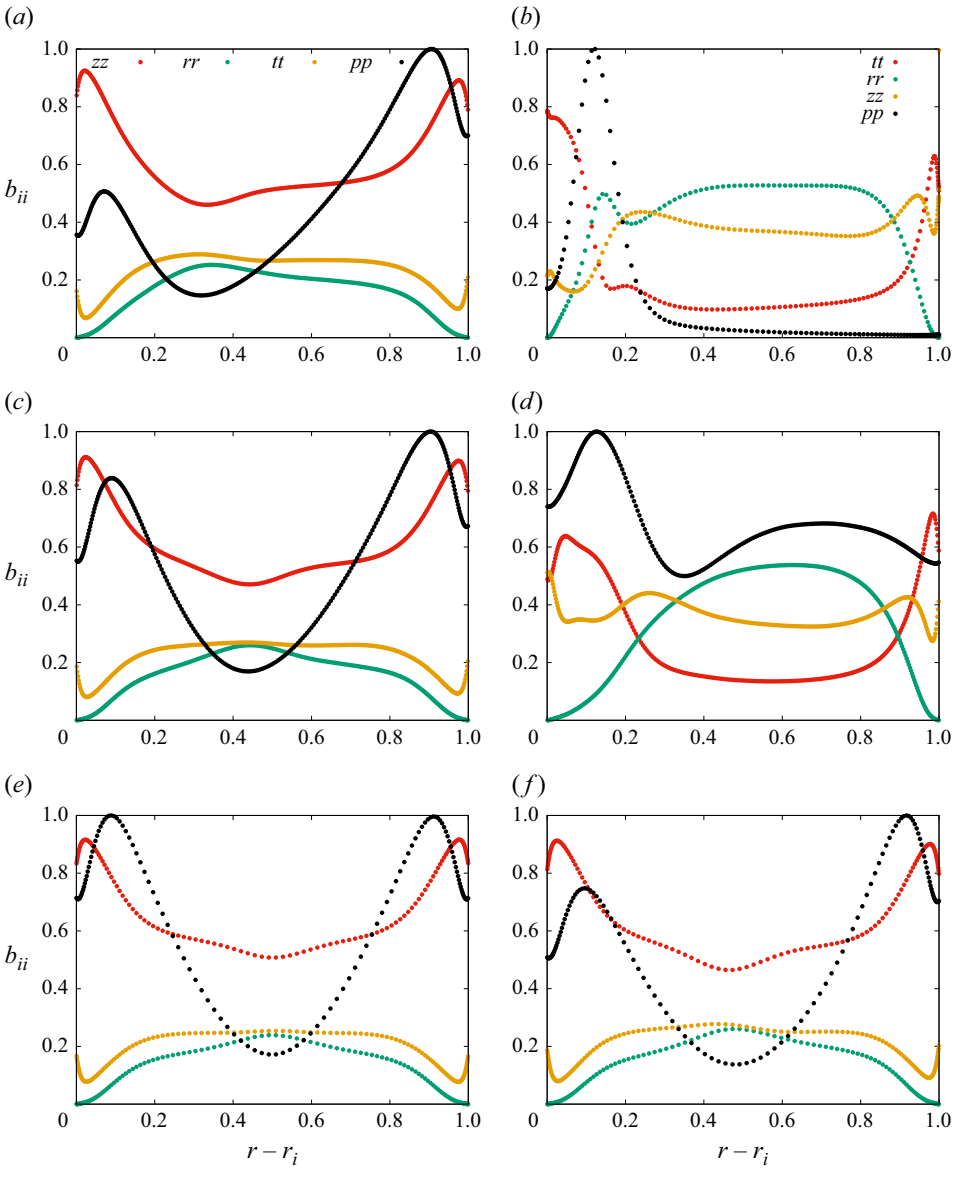

Figure 6. Diagonal components of the anisotropy tensor (streamwise in red, wall-normal in green, and spanwise in orange) and fluctuating pressure correlations (in black) scaled by their maximum value versus distance from the inner radius. Left-hand panels correspond to axial flows, and right-hand panels to azimuthal flows, with (a,b) $r_i = 0.125$, (c,d) $r_i = 1$ and (e,f) $r_i = 79.5$.

longitudinal curvature induces major modifications in azimuthal flows. Therefore, the remainder of this paper will focus on azimuthal flows only.

3.4. *Budgets of TKE*

In the previous discussion, greater emphasis was placed on azimuthal flows, with a special focus on how flow statistics change near the inner wall as the curvature increases. Important insights into these flow modifications can be gained through the analysis of the

TKE budgets. For azimuthal flows, the transport equation for the TKE is

$$0 = -C_\theta \underbrace{-\frac{\overline{v_r' v_z'}}{r}\frac{\mathrm{d}(\overline{v_z} r)}{\mathrm{d}r} - \frac{\overline{v_r' v_\theta'}}{r}\frac{\mathrm{d}(\overline{v_\theta} r)}{\mathrm{d}r}}_{P_{\theta S}} \underbrace{-\frac{\overline{v_\theta' v_r'}}{r}\overline{v_\theta} + \frac{\overline{v_\theta' v_\theta'}}{r}\overline{v_r}}_{P_{\theta C}} \underbrace{-\frac{1}{r}\frac{\mathrm{d}\overline{v_r' K' r}}{\mathrm{d}r}}_{T_\theta} \underbrace{-\frac{1}{r}\frac{\mathrm{d}\overline{v_r' p' r}}{\mathrm{d}r}}_{\Pi_\theta}$$
$$\underbrace{+\frac{1}{Re}\left[\overline{v_z' \nabla^2 v_z'} + \overline{v_\theta' \nabla^2 v_\theta'} + \overline{v_r' \nabla^2 v_r'}\right] + \frac{1}{Re}\left[\frac{1}{r^2}\left(-\overline{v_\theta' v_\theta'} - \overline{v_r' v_r'} + 2\left(\overline{v_\theta' \frac{\partial v_r'}{\partial \theta}} - \overline{v_r' \frac{\partial v_\theta'}{\partial \theta}}\right)\right)\right]}_{D_\theta}, \tag{3.4}$$

where C_θ, the convective contribution, is zero as $\overline{v_r} = 0$, P_θ is the production, D_θ is the total dissipation, T_θ is the transfer due to triple velocity correlations, and Π_θ is the transfer due to pressure–velocity correlations. The production term P_θ can be decomposed into two components: $P_{\theta S}$, which is the product of the Reynolds stress and the shear strain rate, and $P_{\theta C}$, the curvature-related term. Generally, $P_{\theta C}$ provides a positive contribution to the total production. As shown by Liu *et al.* (2022), $P_{\theta C}$ may be the critical factor driving relaminarisation in turbulent pipe flow with streamwise-varying wall rotation, as this term facilitates the transfer of energy from turbulence to the circumferential mean flow. In axial flows, $P_{\theta C}$ is relatively large at very small values of r_i, but becomes negligible when $r_i \geqslant 1$. The inset of figure 7(*a*) illustrates that $P_{\theta C}$ exceeds P_θ near the wall, and it is insufficient to offset the negative values of $P_{\theta S}$. This imbalance leads to a negative P_θ, as shown in figure 4(*b*), although this effect diminishes for larger r_i. The profiles of each term are depicted in figure 7 for the azimuthal flow cases with $r_i = 0.025$, 0.125, 1 and 79.5. To elucidate the budgets of $\overline{K}$ in the region near the inner wall, a logarithmic scale for $r - r_i$ is employed.

For $r_i = 79.5$ (figure 7*d*), the TKE budgets exhibit a distribution typical of plane channels, featuring a balance between production P_θ (red dots), and total dissipation D_θ (green dots). The peak of total dissipation is located slightly closer to the inner wall compared to the production peak. The triple velocity transfer term T_θ (black dots) indicates an energy transfer from the near-wall region, dominated by ribbon-like structures, towards the adjacent layer, dominated by rod-like structures (Orlandi 2019).

For $r_i = 1$ (figure 7*c*), the contribution of the pressure–velocity correlation Π_θ (purple dots) is still relatively small, albeit greater than for $r_i = 79.5$, and comparable in magnitude to the other terms. Although the semi-logarithmic scale does not illustrate clearly the budgets close to the outer wall, it is evident that the amplitude of each term near the inner wall is markedly lower than at the outer wall. This substantial reduction of all budgets near the inner wall is reflected in the profiles of $\overline{K}$, shown in figure 8 as a function of the distance from the inner wall. For $r_i = 1$ (cyan dots), a near-wall bump is absent near the inner wall, in contrast to the peak observed near the outer wall.

For $r_i = 0.125$ and 0.025 (respectively figures 7*b*,*a*), the budgets of TKE change dramatically. The pressure–velocity correlation term increases to an order of magnitude higher than the production term observed for $r_i = 79.5$. (Note that the vertical axis ranges are different.) This increase is likely associated with the negative production, which draws fluctuations from small to large scales of motion. The large-scale fluctuating pressure interacts with large ejections of radial velocity from the inner wall, leading to a significant gain of TKE. This strong energy gain is subsequently dissipated and partially transferred away from the inner wall region via the triple velocity transfer term. This increase in energy gained and lost results in higher peaks of $\overline{K}$ near the inner wall compared to the outer wall, as is clearly visible in figure 8(*a*) for $r_i = 0.125$ (green dots) and even more markedly for $r_i = 0.025$ (red dots).

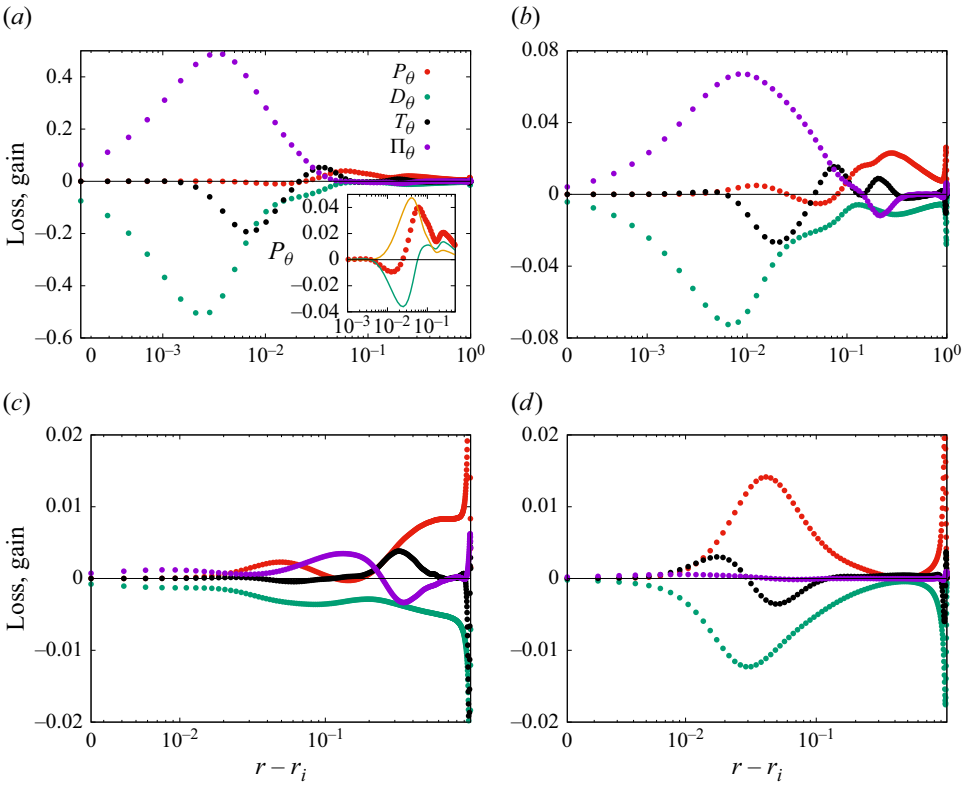

Figure 7. Profiles of each term of the TKE transport equation (3.5) versus the distance from inner radius for azimuthal flow cases with (*a*) $r_i = 0.025$, (*b*) $r_i = 0.125$, (*c*) $r_i = 1$, and (*d*) $r_i = 79.5$. The symbols used for each term are reported in the legend. In the inset of (*a*) are plotted P_θ (red symbols), $P_{\theta S}$ (green lines) and $P_{\theta C}$ (orange lines).

The non-monotonic trend of $\overline{K}$ with r_i is analogous to the C_f trend shown in figure 2(*b*). A comparison of the TKE profiles for azimuthal flows in figure 8(*a*) and for axial flows in figure 8(*b*) reveals that for axial flows, the two peaks of $\overline{K}$ have similar magnitudes; however, the minimum shifts from the centreline towards the inner wall as r_i decreases. The relatively minor changes in the TKE profiles for axial flows near both walls are replicated in the budget profiles, which are not shown here as they do not differ significantly from those observed in canonical wall-bounded flows.

3.5. *Flow visualisations*

As mentioned previously, major changes in the statistics of azimuthal flows, which are particularly pronounced for small values of the inner radius, indicate the presence of distinctive flow structures developing near the inner wall. These structures can be characterised by inspecting flow visualisations after a careful selection of the relevant quantities, essential for obtaining meaningful insights into the flow organisation. According to Orlandi (2013), the wall-normal velocity stress is a crucial quantity in flows over both smooth and rough walls, making the correlation between v_r' and any pertinent quantity a preferred subject of scrutiny. The atypical distribution of the pressure–velocity correlation term in the TKE transport equation, which deviates from the canonical behaviour observed in wall-bounded flows, points to the significant role of

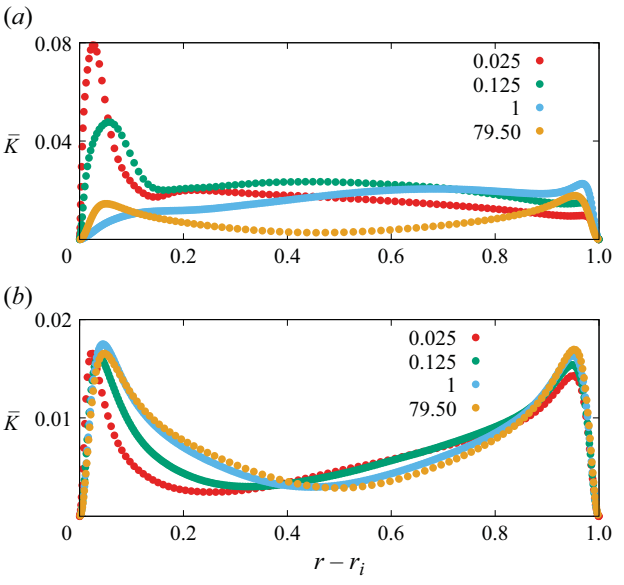

Figure 8. Profiles of mean TKE versus the distance from the inner wall for (a) azimuthal flows and (b) axial flows. The values of the inner radius are reported in the legend.

pressure fluctuations in azimuthal flows. Therefore, special attention should be paid to the correlations between p' and v_r'.

Due to the complexity of three-dimensional surface contours, the flow structures from a single realisation are visualised via planar contours. As for the transverse (r–z) and longitudinal (θ–r) planes, flow contours are obtained through space averages. Specifically, the three-dimensional field of a generic quantity q_{ijk} is averaged along the θ-direction, $\widetilde{q} = \sum_i q_{ijk}/N_\theta$, and along the z-direction, $\widehat{q} = \sum_k q_{ijk}/N_z$, to obtain visualisations in the r–z plane and in the θ–r plane, respectively. Contours of $\widetilde{q}$ and $\widehat{q}$ are scaled by their respective maximum values to emphasise the shape of flow structures. As for the wall-parallel (θ–z) planes, flow contours are displayed both at the centreline and at the radius where Π_θ attains its maximum near the inner wall (see figure 7). In this case, the three-dimensional quantities v_r' and p' are normalised by $\overline{K}^{1/2}$ and $\overline{p'p'}^{1/2}$, respectively. The comparison between the θ–z planes at these two locations provides insights into the increase in the pressure–velocity correlation Π_θ (see (3.5)) as the inner radius decreases. Since wall-parallel planes have a different extent in the θ-direction depending on r_i, the streamwise coordinate has been scaled so that it ranges between 0 and 2π.

For $r_i = 0.025$, the shape of the contours in figure 9(a) indicates that $\widetilde{v_r'}$ is concentrated towards the outer top wall (solid black line) and tends to vanish near the inner bottom wall (solid green line). However, when scaled by $\overline{K}^{1/2}$ (figure 10a), contours of v_r reveal that alternating positive and negative structures with spanwise coherence are present near the inner wall. For pressure, an almost opposite behaviour is observed. Flow structures with large values of $\widetilde{p'}$ form near the inner wall (figure 9c), while they are absent in the outer half of the channel. This difference is quantified in figure 9(e), which shows that for $r_i = 0.025$, pressure oscillations at the inner wall (red line) have significantly higher amplitude than at the outer wall (black line). Conversely, for $r_i = 1$, figure 9(f) shows that pressure oscillations at the two walls are similar, although their overall magnitude is smaller than for $r_i = 0.025$.

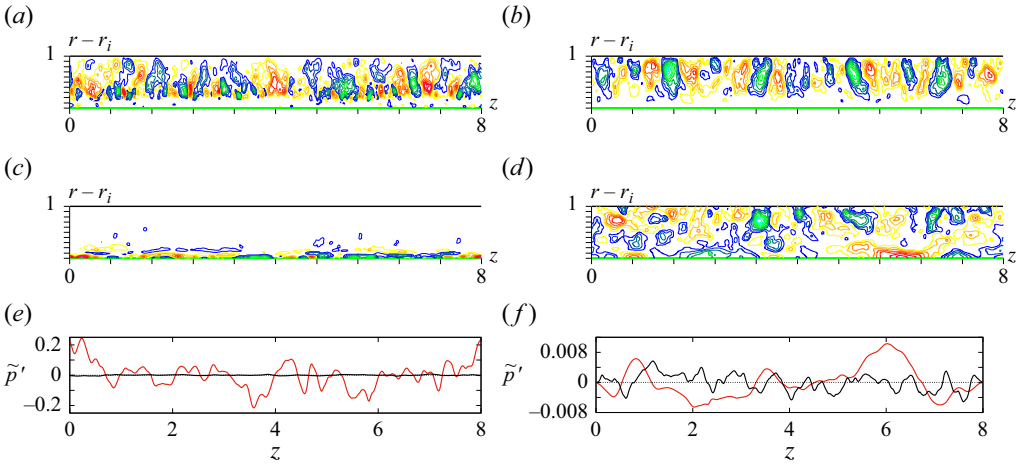

Figure 9. Contours in transverse (r–z) planes of azimuthal flow cases with (a,c) $r_i = 0.025$ and (b,d) $r_i = 1$. Fluctuating radial velocity $\widetilde{v}_r'$ scaled with the maxima (a) $\widetilde{v}_{r\,max}' = -0.25$ and (b) $\widetilde{v}_{r\,max}' = -0.128$. Pressure $\widetilde{p}'$ scaled with the maxima (c) $\widetilde{p}'_{max} = 0.26$ and (d) $\widetilde{p}'_{max} = -0.0137$. The outer wall is at the top, and the inner wall is at the bottom of each plot. Blue, green, cyan represent negative values, and yellow, red, magenta represent positive values, with increments $\Delta = 0.1$. Profiles of $\widetilde{p}'$ on the inner wall (red) and outer wall (black) of (e) $r_i = 0.025$ and (f) $r_i = 1$.

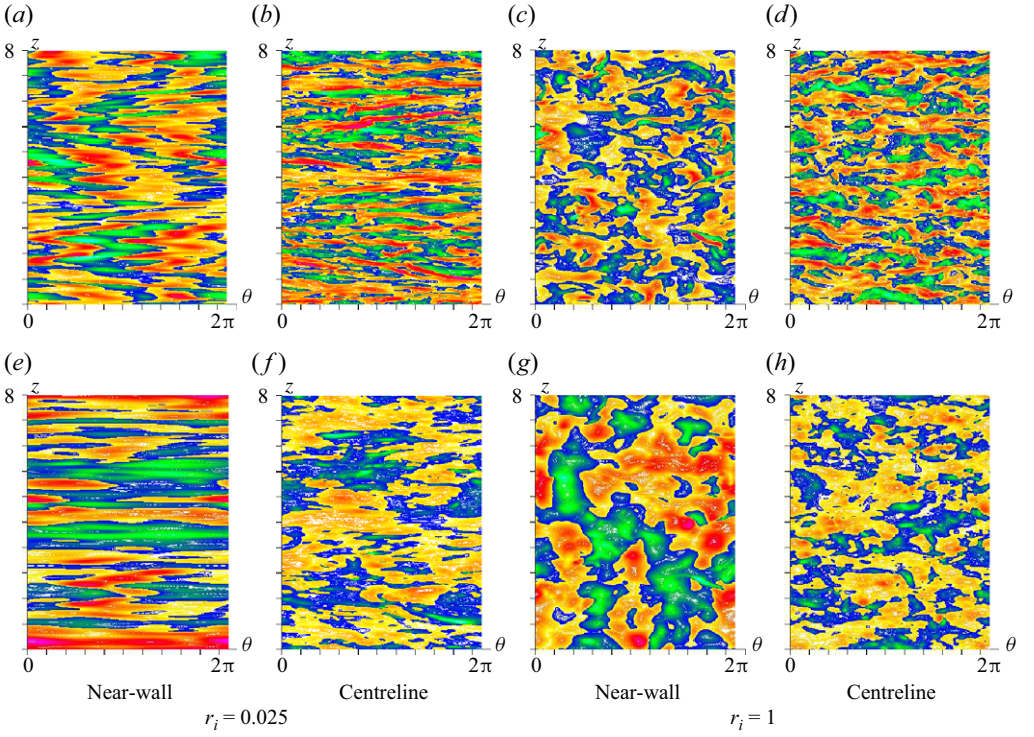

Figure 10. Contours in wall-parallel (θ–z) planes of azimuthal flow cases with (a,b,e,f) $r_i = 0.025$ and (c,d,g,h) $r_i = 1$: fluctuating radial velocity $v_r'/\overline{K}^{1/2}$ (top panels) and pressure $p'/\overline{p'p'}^{1/2}$ (bottom panels). Wall-parallel planes are displayed at (a,c,e,g) the radius of maximum Π_θ and (b,d,f,h) the centreline. Blue, green, cyan represent negative values, and yellow, red, magenta represent positive values, with increments (a) $\Delta = 0.005$, (c) $\Delta = 0.025$, (b,d) $\Delta = 0.06$, (e,g) $\Delta = 0.04$, (f,h) $\Delta = 0.08$. Mean flow is from left to right.

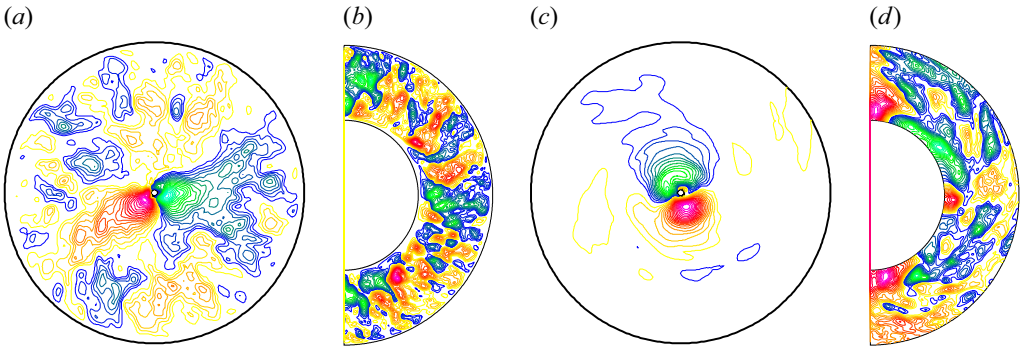

Figure 11. Contours in longitudinal (θ–r) planes of azimuthal flow cases with (a,c) $r_i = 0.025$ and (b,d) $r_i = 1$, and fluctuating (a,b) radial velocity $\widehat{v_r'}$ and (c,d) pressure $\widehat{p'}$, both averaged along the z-direction, scaled by their maximum values: (a) $\widehat{v_r'}_{max} = 0.053$, ($b$) $\widehat{v_r'}_{max} = 0.026$, ($c$) $\widehat{p'}_{max} = 0.092$, ($d$) $\widehat{p'}_{max} = 0.006$. Blue, green, cyan represents negative values, and yellow, red, magenta represent positive values, with increments $\Delta = 0.05$. Mean flow is clockwise.

The spanwise coherence of p' in figure 10(e) is less evident than that of v_r in figure 10(a). Nonetheless, high positive/negative values of p' tend to align with high negative/positive values of v_r, suggesting that a negative correlation exists between the two quantities. Streamwise-coherent structures with alternating positive and negative amplitudes of radial velocity are visible in the wall-parallel plane at the centreline (figure 10b), where the spanwise coherence is reduced. Accordingly, numerous weak patches of $\widehat{v_r'}$ appear in the θ–r plane of figure 11(a) far away from the inner wall, where instead two strong structures are present. A spanwise coherence of p' is undetectable in the θ–z plane at the centreline (figure 10f). In fact, contour lines of $\widehat{p'}$ disappear completely in the outer part of the θ–r plane (figure 11c). Two distinct patches of $\widehat{p'}$ are present near the inner wall, shifted by approximately $\pi/2$ with respect to the two $\widehat{v_r'}$ patches.

For the flow case with $r_i = 1$, a similarity in the $\widetilde{v_r'}$ contours (figure 9b) is observed, with those of the case with $r_i = 0.025$ (figure 9a) near the inner wall. Farther from the wall, the radial velocity is organised in streamwise-coherent structures, which are pushed towards the outer wall and are larger than those at $r_i = 0.025$. These structures are also visible in the wall-parallel plane at the centreline (figure 10d), and are caused by longitudinal vortices that originate from centrifugal instabilities (Soldati *et al.* 2025). Both spanwise and streamwise coherence of v_r are reduced near the inner wall, as is visible in figure 10(c). This suggests a tendency of the flow towards more isotropic conditions near the inner wall, which we already noticed from the profiles of the anisotropy tensor diagonal components and from the reduction of all terms in the TKE budgets equation; see figures 6(d) and 7(c). From the contours in the θ–z plane (figure 11b), numerous weak patches of $\widehat{v_r'}$ appear, increasing from a single pair at $r_i = 0.025$ (figure 11a) to a higher number, which is challenging to evaluate exactly due to the azimuthal convection of these flow patterns. From the pressure contours in the transverse and wall-parallel planes of figures 9(d) and 10(g), it appears that pressure is characterised by a strong spanwise coherence near the inner wall, which reduces at the centreline (figure 10h). This behaviour is reflected in the longitudinal plane (figure 11d), where large flow patterns are visible near the inner wall, and tend to break up towards the outer wall.

3.6. *Correlation between radial velocity and pressure*

The increase in the pressure–velocity correlation Π_θ (see (3.5)), identified as a key feature of azimuthal flows with small inner radius, can be explained by analysing the correlations

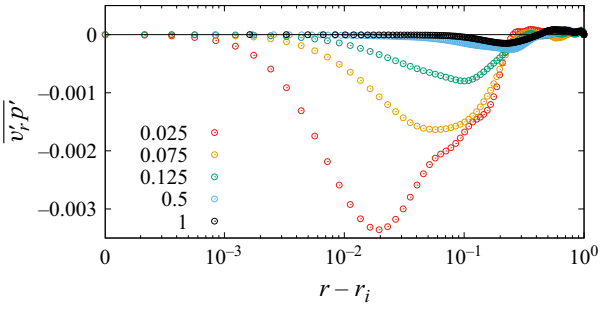

Figure 12. Correlation between fluctuating radial velocity and pressure versus distance from the inner wall for azimuthal flows. The values of r_i are reported in the legend.

between the fluctuating radial velocity and pressure. Additionally, these correlations can provide valuable insights for quantifying the number of spanwise-coherent flow patterns.

Figure 12 illustrates the trend of $\overline{v_r' p'}$ as a function of the distance from the inner wall, using a semi-logarithmic scale to magnify the region near the inner wall. In the case of smallest inner radius $r_i = 0.025$ (red circles), the prominent peak of $\overline{v_r' p'}$ indicates a strong negative correlation between fluctuating pressure and radial velocity near the inner wall, consistent with flow visualisations. As r_i increases, the peak amplitude decreases sharply, and the peak location shifts further from the inner wall.

This trend can be visualised in figure 13, where the contours of the z-averaged correlations between fluctuating pressure and radial velocity, $\widehat{v_r' p'}$ (scaled by their maximum value), are shown in longitudinal planes. Consistent with the profiles of $\overline{v_r' p'}$, negative (blue) contour lines of $\widehat{v_r' p'}$ are predominant near the inner wall for $r_i = 0.025$ (figure 13*a*), as well as for $r_i = 0.075$ and $r_i = 0.125$ (figures 13*b*,*c*). Further from the inner wall, alternating regions of positive and negative contour lines appear, which are due to the phase shift between the patches of radial velocity (figure 11*a*) and pressure (figure 11*c*). These patches are the footprints of spanwise-coherent flow structures, which are organised in two pairs for $r_i = 0.025$ (figure 13*a*), and three pairs for $r_i = 0.075$ and 0.125 (figures 13*b*,*c*).

For $r_i = 0.5$ and $r_i = 1$ (figures 13*d*,*e*), there is still some negative correlation between $\widehat{v_r'}$ and $\widehat{p'}$ near the inner wall, which tends to become positive towards the outer wall. Qualitatively, the number of flow patches increases with r_i, though their precise quantification from an instantaneous flow field is quite challenging due to the reduced spanwise coherence of these structures for larger values of inner radius. In addition, these patches are convected by the mean flow, and rotate in time around the inner wall, making it tricky to use time averages. A detailed analysis of the spanwise structures can be found in Soldati *et al.* (2025), who provided a more accurate evaluation of their number using velocity spectra and phase averages.

4. Conclusions

In a previous study by our group, direct numerical simulations (DNS) were reported in Soldati *et al.* (2025) for fully developed azimuthal flow in curved channels with mild and strong curvature, namely $r_i = 40$ and $r_i = 0.5$. The study focused on examining variations in flow structures and statistical properties as a function of the Reynolds number, revealing significant changes in the fluid dynamics between the two curvature regimes. One of the

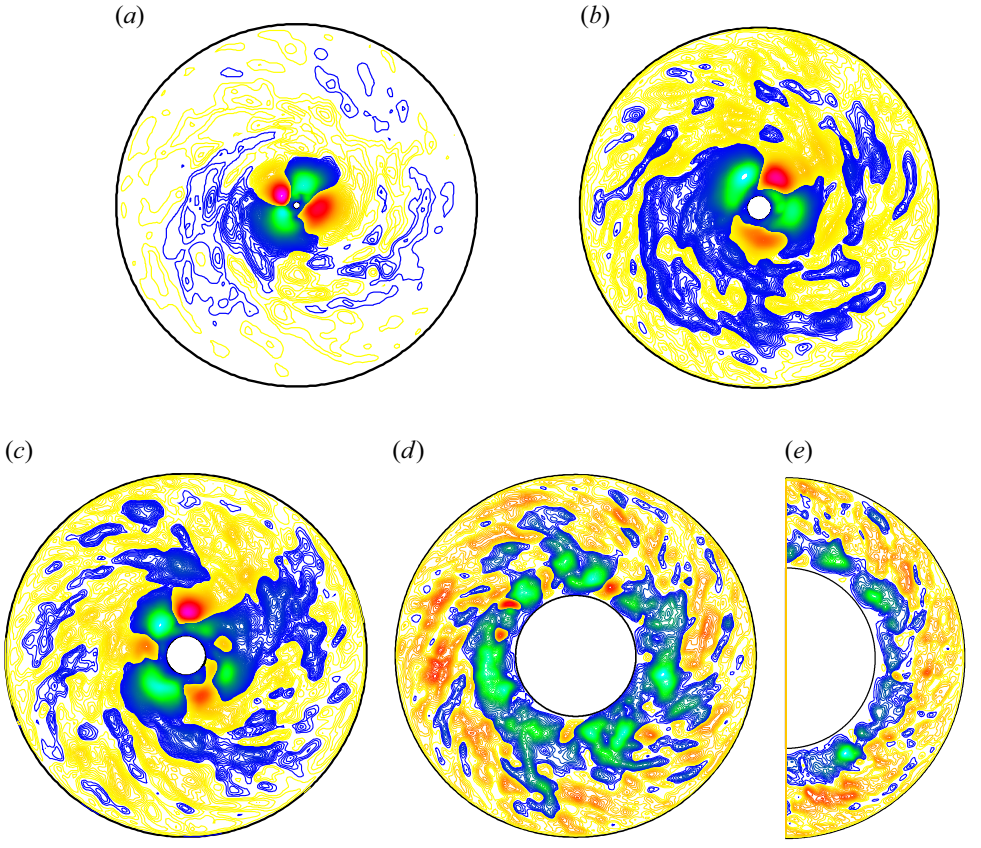

Figure 13. Contours in longitudinal (θ–r) planes of azimuthal flow cases with r_i values (*a*) 0.025, (*b*) 0.075, (*c*) 0.125, (*d*) 0.5, and (*e*) 1; z-averaged correlation between fluctuating radial velocity and pressure ($\widehat{v_r' p'}$). Blue, green, cyan represent negative values, and yellow, red, magenta represent positive values, with increments (*a*) $\Delta = 0.0001$, (*b*,*c*,*d*,*e*) $\Delta = 0.00002$.

key findings was the distinctive flow behaviour near the inner wall of the strongly curved channel, which was shown to be influenced by large-scale spanwise structures.

Those results motivated us to further investigate curved channel flow, an archetypal configuration for studying the effects of longitudinal curvature on turbulence. To develop a more comprehensive understanding of flow over three-dimensional surfaces, we also considered wall curvature transverse to the flow, which in its simplest configuration is flow in a concentric annulus. The geometry of both configurations consists of two concentric cylinders, with the distinction being that the curved channel flow occurs in the azimuthal direction, whereas the annular flow occurs in the axial direction. Through an extensive DNS campaign, we investigated the effects of both longitudinal and transverse curvature on turbulence by varying the inner radius from the large value $r_i = 95.5$ – comparable to that used in the experimental work of Hunt & Joubert (1979) for azimuthal flow – to the extremely small value $r_i = 0.025$, which matches the conditions used by Boersma & Breugem (2001) in axial flow simulations. The bulk Reynolds number was set to $R_b \approx 5000$, based on the bulk velocity and gap width, a value sufficient to ensure fully turbulent conditions (Soldati *et al.* 2025).

The first quantity analysed was the friction coefficient. In axial flows, frictions at the inner wall and at the outer wall monotonically increase and decrease, when curvature

is reduced. Azimuthal flows show a more complex dependence on curvature. For mild curvature, friction at the inner wall is lower than that at the outer wall, as expected due to the stabilising effect of convex curvature. However, the difference between friction at the two walls decreases as the curvature increases, to the point that for strong curvatures, the friction at the inner wall exceeds that at the outer wall. This behaviour allows us to identify four flow regimes, namely: (i) mild curvature for $r_i > 14.5$; (ii) moderate curvature for $1.5 < r_i \leqslant 14.5$; (iii) strong curvature for $0.25 < r_i \leqslant 1.5$; (iv) extreme curvature for $r_i \leqslant 0.25$. The analysis of normal stresses and pressure correlations revealed that the statistics of axial flow in a concentric annulus responds predictably to changes in curvature. In contrast, longitudinal curvature induces significant changes in azimuthal flows, particularly in pressure correlations. For mild curvature, pressure correlations decrease near the inner wall, whereas they increase drastically for strong curvature.

Our findings align with those of Boersma & Breugem (2001) and Bagheri *et al.* (2020), confirming that no regions of negative turbulent kinetic energy (TKE) production are generated in axial flows. In azimuthal flows, however, negative production regions arise due to the displacement between the locations of zero shear and turbulent stress, a phenomenon observed for all values of curvature considered. While the peak of negative production is negligible for mild curvatures, it becomes increasingly pronounced as curvature intensifies, with the peak shifting closer to the inner wall. Negative TKE production is associated with an energy transfer from the small scales of turbulence to the largest scales of motion. In turbulent flows, the pressure field tends to be more coherent at larger scales compared to the velocity field. As a result, pressure fluctuations are expected to exhibit greater coherence near the inner wall, particularly for strong curvature. Indeed, flow visualisations of azimuthal flows revealed spanwise coherence in fluctuating pressure, which interacts with the fluctuating radial velocity. A misalignment between these spanwise structures leads to a strong negative correlation between pressure and radial velocity fluctuations.

The increased correlation between radial velocity and pressure results in a completely different distribution of terms in the TKE transport equation, which has never been observed in wall-bounded turbulent flows. In the region near the inner wall of strongly curved channels, the production term becomes negligible, and TKE is gained instead through pressure–velocity correlations. This significant energy gain is partially transferred away from the inner wall by triple velocity correlations, and is locally dissipated by total dissipation. Notably, the total dissipation is not split into viscous and isotropic contributions, which are in perfect balance at the wall. It is important to note that this complete redistribution of TKE budgets occurs only under conditions of extreme curvature, where the mean TKE is higher near the inner wall than near the outer wall. This is not the case for an inner radius of half the channel height ($r_i = 0.5$), which can be considered as the boundary between strong and extreme curvature. For mild to strong curvature ($r_i > 0.5$), a stabilising effect of convex curvature – leading to reductions in total stress, TKE production, and mean TKE near the inner wall – is observed. However, under extreme curvature conditions ($r_i < 0.5$), the flow structures near the inner wall undergo dramatic changes, resulting in a sudden increase in total stress and mean TKE, and the emergence of a pronounced negative production peak.

While our study is mainly of academic interest, being almost impossible to reproduce in practice, Taylor–Couette flow could be a better candidate for laboratory studies. Specifically, we believe that it could be worthwhile to conduct numerical experiments of Taylor–Couette flow with internal radii as small as 0.02δ, to assess whether the same behaviour of turbulence is herein observed in azimuthal flow. Still, challenges in obtaining accurate measurements of friction factors, velocity profiles and flow visualisations remain

significant. A DNS campaign of Taylor–Couette flow is underway, and the results will be presented in subsequent publications.

Acknowledgements. The results reported in this paper have been achieved using the PRACE Research Infrastructure resource LUMI-C.

Funding. This research received financial support from ICSC-Centro Nazionale di Ricerca in 'High Performance Computing, Big Data and Quantum Computing', funded by European Union-NextGenerationEU.

Declaration of interests. The authors report no conflict of interest.

Data availability statement. All data that support the findings of study are available from the corresponding author upon request.

References

Bagheri, E., Wang, B.-C. & Yang, Z. 2020 Influence of domain size on direct numerical simulation of turbulent flow in a moderately curved concentric annular pipe. *Phys. Fluids* **32** (6), 065105.

Boersma, B.J. & Breugem, W.P. 2001 Numerical simulation of turbulent flow in concentric annuli. *Flow Turbul. Combust.* **86** (1), 113–127.

Brethouwer, G. 2022 Turbulent flow in curved channels. *J. Fluid Mech.* **931**, A21.

Chung, S.Y., Rhee, G.H. & Sung, H.J. 2002 Direct numerical simulation of turbulent concentric annular pipe flow, part 1: flow field. *Intl J. Heat Fluid Flow* **23** (4), 426–440.

Erm, L.P. & Joubert, P.N. 1991 Low-Reynolds-number turbulent boundary layers. *J. Fluid Mech.* **230**, 1–44.

Eskinazi, S. & Erian, F.F. 1969 Energy reversal in turbulent flows. *Phys. Fluids* **12** (10), 1988–1998.

Ghaemi, S., Rafati, S., Bizhani, M. & Kuru, E. 2015 Turbulent structure at the midsection of an annular flow. *Phys. Fluids* **27** (10), 105102.

Hunt, I.A. & Joubert, P.N. 1979 Effects of small streamline curvature on turbulent duct flow. *J. Fluid Mech.* **91** (4), 633–659.

Lee, M. & Moser, R.D. 2015 Direct numerical simulation of turbulent channel flow up to. *J. Fluid Mech.* **774**, 395–415.

Liu, X., Zhu, H., Bao, Y., Zhou, D. & Han, Z. 2022 Turbulence suppression by streamwise-varying wall rotation in pipe flow. *J. Fluid Mech.* **951**, A35.

Moser, R.D. & Moin, P. 1987 The effects of curvature in wall-bounded turbulent flows. *J. Fluid Mech.* **175**, 479–510.

Nagata, M. & Kasagi, N. 2004 Spatio-temporal evolution of coherent vortices in wall turbulence with streamwise curvature. *J. Turbul.* **5** (1), 017.

Nouri, J.M., Umur, H. & Whitelaw, J.H. 1993 Flow of Newtonian and non-Newtonian fluids in concentric and eccentric annuli. *J. Fluid Mech.* **253**, 617–641.

Orlandi, P. 2013 The importance of wall-normal Reynolds stress in turbulent rough channel flows. *Phys. Fluids* **25** (11), 110813.

Orlandi, P. 2019 Turbulent kinetic energy production and flow structures in flows past smooth and rough walls. *J. Fluid Mech.* **866**, 897–928.

Orlandi, P. & Fatica, M. 1997 Direct simulations of turbulent flow in a pipe rotating about its axis. *J. Fluid Mech.* **343**, 43–72.

Patel, V.C. & Head, M.R. 1969 Some observations on skin friction and velocity profiles in fully developed pipe and channel flows. *J. Fluid Mech.* **38** (1), 181–201.

Pope, S.B. 2000 *Turbulent Flows*. Cambridge University Press.

Quadrio, M. & Luchini, P. 2002 Direct numerical simulation of the turbulent flow in a pipe with annular cross section. *Eur. J. Mech. B Fluids* **21** (4), 413–427.

Rehme, K. 1974 Turbulent flow in smooth concentric annuli with small radius ratios. *J. Fluid Mech.* **64** (2), 263–287.

Soldati, G., Orlandi, P. & Pirozzoli, S. 2025 Reynolds number effects on turbulent flow in curved channels. *J. Fluid Mech.* **1007**, A28.

Verzicco, R. & Orlandi, P. 1996 A finite-difference scheme for three-dimensional incompressible flows in cylindrical coordinates. *J. Comput. Phys.* **123** (2), 402–414.